







Modular thermal Hall effect measurement setup for fast-turnaround screening of materials over wide temperature range using capacitive thermometry

Cite as: Rev. Sci. Instrum. **90**, 103904 (2019); <https://doi.org/10.1063/1.5108512>

Submitted: 29 April 2019 . Accepted: 22 September 2019 . Published Online: 15 October 2019

Ha-Leem Kim , Matthew John Coak , J. C. Baglo , Keiron Murphy , R. W. Hill, Michael Sutherland, M. Ciomaga Hatnean , Geetha Balakrishnan, and Je-Geun Park 



View Online



Export Citation



CrossMark

ARTICLES YOU MAY BE INTERESTED IN

[SquidLab—A user-friendly program for background subtraction and fitting of magnetization data](#)



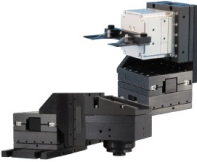
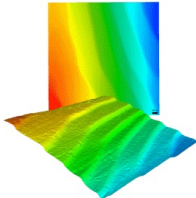
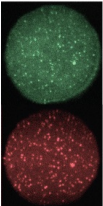
Review of Scientific Instruments **91**, 023901 (2020); <https://doi.org/10.1063/1.5137820>

[Apparatus for Seebeck coefficient measurement of wire, thin film, and bulk materials in the wide temperature range \(80–650 K\)](#)

Review of Scientific Instruments **90**, 104901 (2019); <https://doi.org/10.1063/1.5116186>

[A modular point contact spectroscopy probe for sub-Kelvin applications](#)

Review of Scientific Instruments **90**, 103903 (2019); <https://doi.org/10.1063/1.5119372>

	<p>Nanopositioning Systems</p> 	<p>Modular Motion Control</p> 	<p>AFM and NSOM Instruments</p> 	<p>Single Molecule Microscopes</p> 
---	--	--	---	--

Modular thermal Hall effect measurement setup for fast-turnaround screening of materials over wide temperature range using capacitive thermometry

Cite as: Rev. Sci. Instrum. 90, 103904 (2019); doi: 10.1063/1.5108512

Submitted: 29 April 2019 • Accepted: 22 September 2019 •

Published Online: 15 October 2019



View Online



Export Citation



CrossMark

Ha-Leem Kim,^{1,2}  Matthew John Coak,^{1,2,3,a)}  J. C. Baglo,⁴  Keiron Murphy,⁴  R. W. Hill,^{4,5}
Michael Sutherland,⁴ M. Ciomaga Hatnean,³  Geetha Balakrishnan,³ and Je-Geun Park^{1,2,a)} 

AFFILIATIONS

¹Center for Correlated Electron Systems, Institute for Basic Science, Seoul 08826, South Korea

²Department of Physics and Astronomy, Seoul National University, Seoul 08826, South Korea

³Department of Physics, University of Warwick, Coventry CV4 7AL, United Kingdom

⁴Cavendish Laboratory, University of Cambridge, J. J. Thomson Ave., Cambridge CB3 0HE, United Kingdom

⁵Department of Physics and Astronomy, University of Waterloo, Waterloo, Ontario N2L 3G1, Canada

^{a)}matthew.coak@warwick.ac.uk and jgpark10@snu.ac.kr

ABSTRACT

We demonstrate a simple and easy-to-build probe designed to be loaded into a widely available Quantum Design Physical Properties Measurement System (PPMS) cryostat, with a detachable shielded sample puck section and robust heat sinking of three pairs of coaxial cables. It can be in principle used with any low-temperature cryostat. Our modular puck design has a radiation shield for thermal isolation and protection of the delicate sample space while handling and allows any variety of experimental setup benefiting from shielded coaxial wiring to be constructed on a selection of sample pucks. Pucks can be quickly and easily switched, and the system makes use of the simple yet extremely stable temperature and magnetic field control of the easy-to-use PPMS system. We focus on a setup designed for measurements of the thermal Hall effect and show that this system can yield unprecedented resolution over a wide temperature range and with rapid sample mounting or changing—allowing a large collection of potential samples to be screened for this novel physics. Our design aims to make these sensitive but challenging measurements quick, reliable, cheap, and accessible, through the use of a standard, widespread base cryostat and a system of modular removable sample stage pucks to allow quick turnaround and screening of a large number of candidate samples for potential new thermal Hall physics.

Published under license by AIP Publishing. <https://doi.org/10.1063/1.5108512>

I. INTRODUCTION

Measurement of thermal transport properties has been widely used to probe the ground state excitations of physical systems for much of the history of condensed matter physics. However, the measured total thermal conductivity of a given material involves contributions from multiple excitation channels and is also strongly affected by convoluted scattering of the quasiparticles. Thus, analysis of the thermal conductivity data involves separation of the individual contributions, and thorough mapping of the field and temperature dependence of the thermal conductivity is necessary.

In complicated systems such as frustrated magnets and strong phonon-scattered systems, measurements of thermal conductivity alone do not yield definitive conclusions due to the perplexing entanglement of various contributions.

Thermal Hall conductivity measurements have recently started to be used as a novel and powerful tool for probing specific excitations, because of their unusual physical realization. For instance, thermal Hall conductivity experiments successfully revealed the existence of fractionalized excitations in quantum spin ice and quantum spin liquid materials,^{1–6} and the magnon band topology has been probed via thermal Hall effect (THE) measurements.^{7–9}

Moreover, the strong skew scattering of phonons, which leads to the phonon Hall effect, has been revealed from THE experiments.^{10–12} Because of its power toward understanding the peculiar characters of fundamental excitations, numerous theoretical works related to the thermal Hall effect have been published in recent years,^{13–21} and an increasing number of high-profile experiments are utilizing this exciting new technique.

However, measured and theoretically calculated thermal Hall conductivity values in insulators are typically in the range 10^{-3} to 10^{-4} W K⁻¹ m⁻¹ and additionally require a high magnetic field to induce measurable thermal Hall signals. Thus, measurement of the THE requires precise temperature measurement with a typical scale of a few milliKelvin or less, under high magnetic fields. Additionally, the long measurement time typically required necessitates fine temperature stability and proper thermal isolation for both thermometers and the sample.

Early experiments to measure the THE employed resistive thermometers such as ruthenium oxide, Cernox, and Chromel-Constantan thermocouples.^{1–11} Since these are subject to significant magnetoresistance at low temperature, precise measurement of temperature in high fields requires extensive magnetic field calibration. Moreover, such thermometers by their nature induce self-heating while being measured, potentially upsetting delicate heat flows. To resolve these difficulties and to make THE measurements practical for a wide range of temperature, the use of SrTiO₃ capacitive thermometers has recently been demonstrated.²² SrTiO₃ (selected for the anomalously high and smooth dielectric constant) thermometers have vanishingly low self-heating and are unaffected by magnetic field, avoiding the need for time-consuming and challenging calibrations with both temperature and field that resistive thermometers require. Capacitance can additionally be measured to exceptional precision, provided that the correctly shielded wiring environment is prepared. These features are all ideal for THE measurements.

In this work, we describe our implementation of a highly sensitive THE measurement setup making use of SrTiO₃ thermometry designed to be loaded into the widely available PPMS cryostat from Quantum Design. We outline the detailed design of the sample probe and detachable sample stage pucks, theoretical calculations of resolution and competing heat channels, experimental performance, and example THE measurement data using a reference sample Tb₂Ti₂O₇. The use of an unmodified PPMS as a base cryostat makes our setup stand apart from the previously reported designs, typically purpose built for a specific refrigerator. Our design aims to make these sensitive measurements quick, reliable, cheap, and accessible through the use of a standard, widespread base cryostat and a system of modular removable sample stage pucks to allow quick turnaround and screening of a large number of potential samples for new thermal Hall physics. The modular puck design has the additional benefit of allowing any other measurements requiring coaxial wiring, such as dielectric constant, proximity-detector-oscillator, or capacitive spin Nernst effect experiments.

II. STEADY STATE THERMAL HALL EFFECT MEASUREMENTS

As shown in Fig. 1, to make measurements of the thermal Hall effect, five thermal contacts are made to a planar, crystalline,

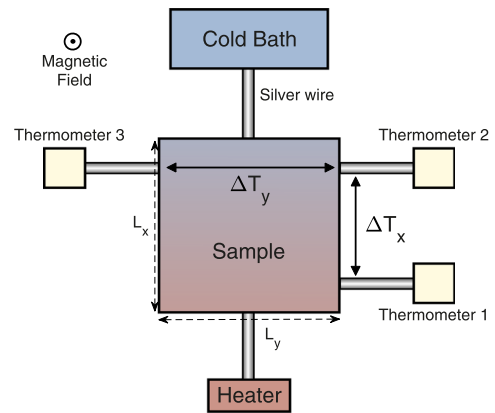


FIG. 1. Schematic outlining the geometry and concept of thermal Hall effect measurements.

sample and thermal connections made to a heater, three thermometers, and the cryostat cold bath. The experiment must be carried out in high vacuum, and all elements shown ought to be isolated from any other heat sources or baths as much as possible, as well as connected to the sample via very high thermal conductances, to rule out competing heat currents. With the heater disabled, the sample can be expected to equilibrate to a temperature close to that of the cold bath (ideally equal to it with no heat leaks) and all thermometers would read this same temperature. This mode of operation can in fact be used to calibrate the thermometers initially. When the resistive heater is enabled for the measurements by passing DC current through it and sufficient time is given for the system to equilibrate, a thermal gradient will be set up along the sample from the heater to the cold bath (x direction in Fig. 1). The readings of the three thermometers then give the linear and transverse temperature differences across the sample ΔT_x and ΔT_y .

The general form of Fourier's law of heat conduction for an anisotropic material in two dimensions (we assume a thin sample and that no thermal gradients develop in the z out-of-sample-plane direction) employs a thermal conductivity tensor $\bar{\kappa}$ to give the directional heat flux per unit area \vec{J} when a steady state heat differential $-\nabla T$ is set up across the sample,

$$\begin{pmatrix} J_x \\ J_y \end{pmatrix} = \begin{pmatrix} \kappa_{xx} & \kappa_{xy} \\ -\kappa_{xy} & \kappa_{xx} \end{pmatrix} \begin{pmatrix} \partial_x T \\ \partial_y T \end{pmatrix}. \quad (1)$$

Conventionally, heat is expected to flow only along temperature gradients, and so off diagonal elements in $\bar{\kappa}$ (i.e., κ_{xy}) will be zero and a simpler expression recovered for thermal conductivity. Applying magnetic field along the z axis can, however, lead to heat current transverse to the zero-field thermal gradient (here applied along the x axis)—the thermal Hall effect. This is directly and simply analogous to the electronic Hall effect where magnetic deflection of electrons or holes leads to a transverse voltage developing but instead with the heat-carrying quasiparticles. The desired values in a thermal Hall experiment are κ_{xy} and κ_{xx} as a function of applied field at a fixed cold bath temperature— κ_{xx} is required to extract κ_{xy} and

for calculation of Hall angle. Experimentally, we measure temperature differences along the applied heat current and perpendicular to it, ΔT_x and ΔT_y —the desired thermal conductivity coefficients can then be found from these values as in Ref. 23,

$$\kappa_{xx} = \frac{PL_x}{(\Delta T_x)L_yL_z}, \quad (2)$$

$$\kappa_{xy} = \kappa_{xx}^2 \frac{L_z(\Delta T_y)}{P}, \quad (3)$$

given the steady-state heater power P and sample dimensions L_x , L_y , and L_z as defined in Fig. 1. The above equations are valid when $\kappa_{xy} \ll \kappa_{xx}$, which is the usual case in insulating systems.

As phonons or other heat-carrying neutral quasiparticles do not directly interact with magnetic field, the thermal Hall effect is typically a very weak, second-order effect. A useful general and sample-independent gauge of the magnitude of the thermal Hall effect in a given material is the thermal Hall angle ratio κ_{xy}/κ_{xx} . If we assume roughly square sample geometries, this is then a measure of signal size independent of heater power, temperature, longitudinal thermal conductivity, and so on. κ_{xy}/κ_{xx} is generally observed to be on the order of 10^{-3} to 10^{-4} ²⁴ for the insulating systems of interest here, and hence, ΔT_y will be on the order of milliKelvin or less for typical, practical ΔT_x values below 5% of sample temperature.

As the thermal contacts to the sample crystal will necessarily be of finite size and imperfectly positioned, the measured transverse heat data will contain a small contribution from the linear heat current, and vice versa. Completely analogous to the electronic Hall effect case, we can use the analysis technique of data symmetrization to separate the two contributions into pure κ_{xx} and κ_{xy} terms. Linear thermal conductivity κ_{xx} will be independent of the field direction ($+z$ or $-z$) and so will manifest as a symmetric, even function of applied field $B = \mu_0 H$. The transverse, thermal Hall, term κ_{xy} will be an odd function of B , as the reversing field must reverse the deflection direction. Data can be collected from $-B_{max}$ to B_{max} , split into the negative and positive sections, and summed or subtracted to obtain the symmetric and antisymmetric components of each signal, e.g., $\Delta T_y^{asym} = \frac{1}{2}(\Delta T_y(B) - \Delta T_y(-B))$. For the antisymmetric thermal Hall signal, this carries the benefit of removing any small constant temperature offset between the thermometers due to any such systematic error, including in calibration.

III. PROBE DESIGN AND ELECTRONICS

A. Probe design

An image and schematic of the full probe assembly is shown in Fig. 2. The probe is designed to be loaded into a Quantum Design PPMS helium cryostat, making use of its temperature and magnetic field control but using external wiring, electronics, and the vacuum system. It can also potentially be used together with any standard low-temperature cryostat of equivalent bore. Capacitive thermometers are used, necessitating the provision of shielded coaxial wiring into the sample space. Three pairs of Lakeshore type SS miniature coaxial wires are wound around a central stainless steel hollow rod

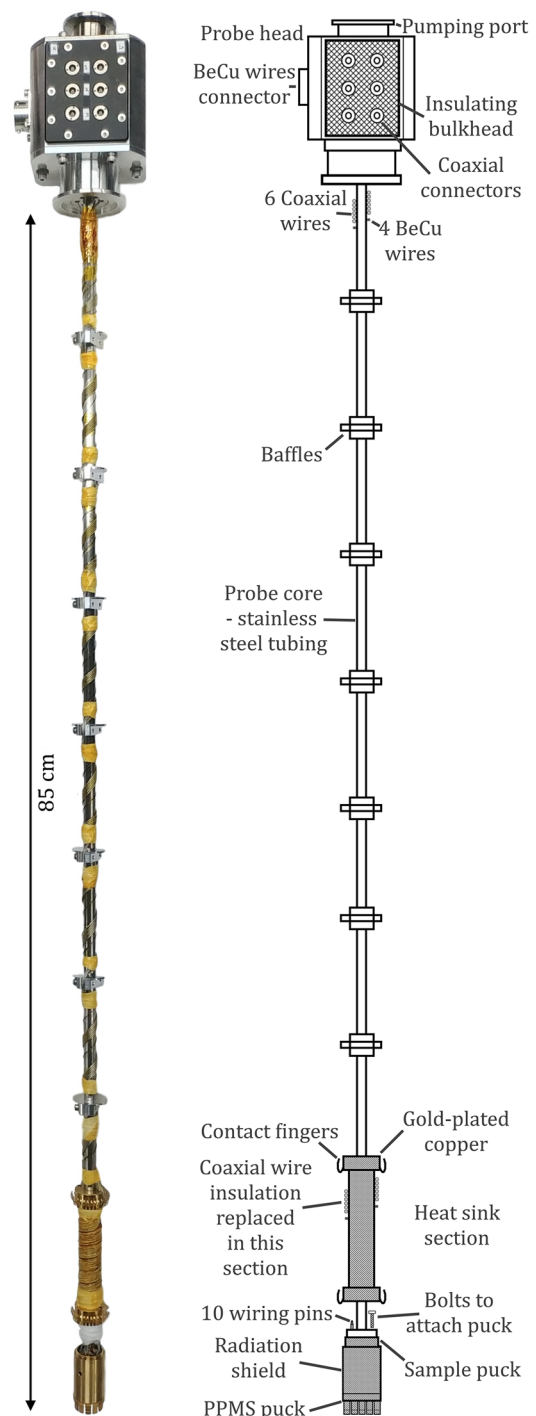


FIG. 2. Photograph and schematic of the full probe.

with detachable steel baffles. These wires are selected for their minimal cross section and braided stainless steel construction, minimizing heat flow from the room-temperature probe head down to the sample environment. LEMO brand hermetic coaxial connectors

terminate these wires at the probe head, mounted on a plastic board to isolate the shield connections from the probe body. Four $90\ \mu\text{m}$ beryllium-copper unshielded wires, in twisted pairs, are additionally run down the length of the probe for connections to the heater. A detachable sample puck section and radiation shield are mounted onto the lower end of the probe (Fig. 3) and terminated in the circular prongs of a standard PPMS puck from Quantum Design to engage into the PPMS cold bath—but with no wiring connections to it. As the probe must engage with the PPMS cold bath at the base and the vacuum flanges at the head, the position of the probe head can be finely adjusted to ensure a matching length—the head is clamped to the core with radial grub screws.

As the system is designed for operation over a wide temperature range (~ 2 to $250\ \text{K}$), the internal PPMS high-vacuum sorption option is not used—instead, a high-throughput turbo-molecular pump is attached to a pumping port in the upper face of the probe head, and experiments are carried out under constant pumping. Base vacuum pressure is typically 4×10^{-7} mbar. To prevent excess heat being trapped in thermally insulating areas of the setup, the probe is cooled in the helium exchange gas of normal PPMS operation, and then, pumping begins once temperatures are stable.

A key component of the probe design is the gold-plated oxygen-free copper heat sink section, placed close to the bottom of the

probe—see Fig. 4(c). The steel probe core and coaxial wires are designed to minimize heat leaks from room temperature, but the dielectric layers and protective sheathing of coaxial cables prevent easy heat sinking. Additionally, the top-loading design of the PPMS cryostat dictates that thermal connection to the cold bath is at the very bottom of the assembly—but wiring and heat leaks are coming from the top, leading to unique engineering challenges. The heat sink section is bounded with spring-loaded beryllium-copper contact fingers laser welded around its outer circumference prior to gold plating. These provide a strong and stable thermal connection to the PPMS chamber walls in the sample region—clamping the heat sink to the cold bath temperature. To facilitate easy heat exchange between the wiring and the heat sink while maintaining electrical isolation between the wires' shields and the probe body, the clear plastic protective outer layer of each coaxial wire was stripped away for the 30 cm length wrapped around the heat sink section. The surface of the heat sink was coated with a thin layer of cigarette paper soaked in General Electric (GE) varnish, extensively diluted with ethanol. Similar GE varnish and paper insulation were wound around the stripped section of each cable. The cables were then wound tightly around the heat sink, held in place, and additional GE varnish was painted over the whole to form a thermal bond while keeping electrical insulation. For an ideal three-terminal

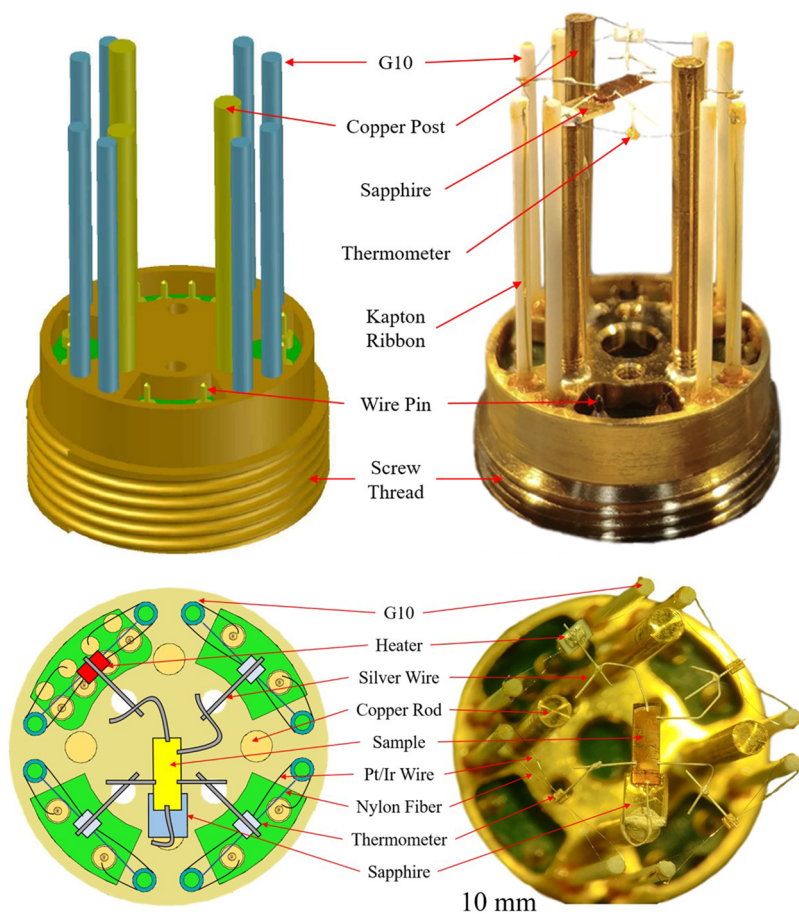


FIG. 3. Drawings and photographs of the measurement puck design, including the mounted sample, heater, and thermometers. This puck is bolted onto the base of the probe, after being covered by the radiation shield which screws onto the threads shown. G10 fiberglass supports, nylon fibers, Kapton ribbons, and Pt/Ir wires ensure thermal isolation of all components, excluding the sample cold bath connection, which is made through a sapphire wafer bonded to one of the vertical copper posts.

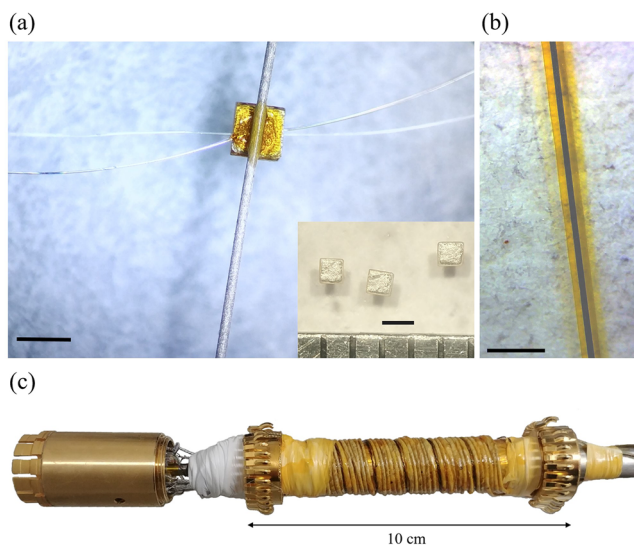


FIG. 4. (a) Photographs of SrTiO₃ thermometers, after making all contacts and mounting on silver wire and on nylon support fibers, and (inset) after evaporating gold electrodes and coating with silver-loaded epoxy. (b) An example gold-plated Kapton ribbon. Scale bars are 1 mm. (c) Heat sink section of the probe, with attached puck and radiation shield.

capacitance measurement, the coaxial shields should be connected only at the sample position, so they are kept isolated at the heat sink stage. Prototype measurements without this crucial heat sink section exhibited Kelvin-level thermal drifts in each thermometer due to heat leaks over periods of days, rendering accurate measurements near-impossible.

B. Sample stage puck

The sample puck section displayed in Figs. 2–4 allows the sample and thermometry wiring and thermal isolation apparatus to be worked on separately from the probe. This puck is fixed to the lower end of the probe's steel core section by three bolts, and gold-coated pins around its circumference (Fig. 3) make electrical connections to the six thermometer and four heater wires. A gold-plated copper radiation shield, integrated onto a standard PPMS puck base (with no electrical pins, only the copper shell) then screws over the sample puck. This ensures stability and isolation from thermal radiation and forms the main thermal connection to the PPMS cold bath. Two holes are drilled into its side to allow the interior to be evacuated. The radiation shield additionally provides mechanical protection to the delicate wiring within, allowing the puck to be handled, mounted, and stored safely. The modular nature of the puck allows multiple experiments to be set up in advance of measurement, spares to be available, and additionally for entirely different experimental setups to be measured on the same probe—such as dielectric measurements or frequency dependent techniques such as proximity detector oscillators²⁵ or capacitive spin Nernst effect measurements,²⁶ which are not possible in a PPMS without such a setup.

Care has been taken to avoid any magnetic components in the construction of the sample pucks as these could influence the local

magnetic field of the sample. Gold-plated copper is the main material, and brass bolts and fittings are used. Vertical copper posts screw into the puck base at the bottom and engage with the radiation shield at the top, forming a strong link to the cold bath—the sample “cold” connection is made to one of these; see Fig. 3. Thin fiberglass posts are mounted alongside these. The purpose of the fiberglass posts is to thermally isolate the elements they support from the cold bath. For the same reason, the thermometers and heater are mounted on thin nylon fibers strung between the top of these fiberglass posts. To make electrical connections to the thermometers and heater while minimizing heat leaks, a combination of 25 μm platinum/iridium wire and specially prepared gold-coated Kapton ribbon is attached to the fiberglass supports. The Kapton ribbons were cut from a 13 μm Kapton film, then all but a thin central region masked off, and 5 nm of titanium followed by 30 nm of gold evaporated onto the surface. This results in a robust and easily handled cable with a resistance around 250 Ω and vanishingly low thermal conductance—discussed in more detail in Sec. IV B. Connections between these ribbons and the Pt/Ir wires were formed by silver-loaded epoxy, and the wires were soldered directly to the pins of the puck.

The thermometer and heater assemblies are permanently mounted on the puck—the sample can easily be switched without disturbing them to allow for quick turnaround and screening of a wide number of samples. Silver wires attached to the sample are joined to those mounted on the thermometers and heater with removable silver-loaded epoxy. Initially, this was the only mechanical support for the free-hanging sample, but it was found that forces from magnetic field could move or rotate the sample crystal. A horizontal sapphire plate was added to the top of one of the copper posts; the sample is attached to this with GE varnish to form the cold bath link and prevent any movement. An additional silver wire connection is formed from the sample surface at this point to the copper post to ensure the best thermal link achievable.

C. Thermometry

To avoid the twin problems of thermometer self-heating and magnetoresistance in high fields, SrTiO₃ capacitive thermometers in parallel-plate geometry were used. The thermometer arrangement is shown in Fig. 4(a). SrTiO₃ wafers of thickness 0.1 mm, both sides polished, were purchased from the MTI Corporation, United States, and cut to $1 \times 1 \text{ mm}^2$ with a diamond wheel. Further development has shown better low-temperature performance from wafers purchased from Crystal GmbH, which should be noted. A 50 nm layer of gold was evaporated onto the two carefully cleaned capacitor faces in turn, with a foil mask to prevent gold encroaching on the edges and sides, as detailed in Ref. 27. The faces were then additionally coated in silver-loaded epoxy [see Fig. 4(a) inset], and Pt/Ir wires were bonded to them with the same. To avoid leads moving under magnetic field changes and vacuum pumping, $\sim 10 \mu\text{m}$ diameter nylon support fibers were strung between the fiberglass posts and attached to the thermometers. This construction keeps the position of the thermometers fixed—movement of the thermometer and wiring can affect the measured capacitance value. 125 μm silver wire was attached to the side of the thermometer, electrically isolated via GE varnish, to make the thermal connection between the thermometer and sample. Calibration of the measured capacitance values into temperature was done *in situ* with the heater disabled

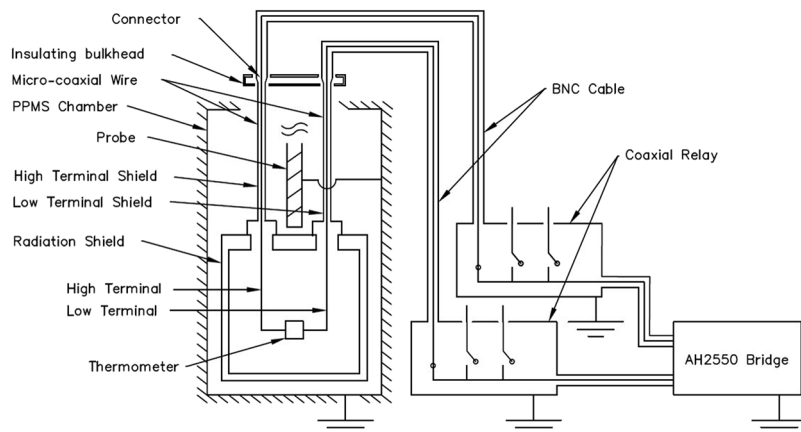


FIG. 5. Schematic outlining the wiring connections used. The shields of the coaxial wires are connected to the radiation shield, which is in turn isolated from the probe body and from the PPMS puck connector. A plastic insulating bulkhead ensures that the coaxial connector shields are likewise isolated from the probe head and body.

prior to each measurement. While the PPMS temperature control uses standard resistive thermometry and sensor readings are hence affected by magnetic fields, we have verified through zero-heater-power measurements that the effect is to raise or lower the overall sample temperature, with no discernible effect on sample temperature differences. The sample average temperature deviation was below 0.2% for the tests carried out; this has a negligible effect on the thermal transport coefficients and hence the experimental signal.

D. Heater

A 15 k Ω resistive chip heater was used (CPF0805B15KE1 from TE Connectivity), with typical DC currents of order 100 μ A. To reduce the heater's thermal mass, its dielectric substrate was polished down to 300 μ m thickness. The heater setup is equivalent to that of the thermometers—two Pt/Ir wires from its contact pads are joined to Kapton ribbons and hence to the probe wiring and the heater is mechanically supported by nylon fibers. The temperature dependence of the resistance was measured in a four-terminal configuration prior to measurements and found to yield a less than 1% change in the resistance value down to 2 K. This change is compensated for in calculating the heater power. The heater is connected in a two-terminal configuration for thermal Hall measurements. Heater power was chosen so that the temperature gradient along the longitudinal direction was kept smaller than 5% of the sample temperature.

E. Electronics

The capacitance values of the three thermometers are measured using an Andeen-Hagerling 2550A 1 kHz capacitance bridge (AH Bridge) and a pair of Universal Switching Corporation URS74004 relays to switch between the three measurement channels. Excitation voltage is set at 0.5 V, and the AH Bridge "Average Time" setting for each measurement is set to option 9 (corresponding to around 7 s measurement duration). The average time or time constant has, of course, a significant effect on the measurement resolution. We use this maximal value throughout all the data presented in this work as there is no real advantage in faster data acquisition here—data are collected in a steady field and temperature state. The use

of relays, as well as avoiding the need for three capacitance bridges, was found to give better noise performance than simultaneous measurements on multiple identical bridges—just as suggested by the Andeen-Hagerling documentation. The use of a relay does, however, mean that temperature measurements are acquired in a sequence rather than simultaneously. As measurement points were taken at fixed, stable temperatures and fields, this does not lead to reduced performance, and the cold bath temperature values were recorded (averaging 10 readings from the PPMS thermometry) before and after each thermometer reading, as well as the time to allow later interpolation of data if necessary. The heater current was supplied by a Keithley 2410 Source Meter, using twisted pairs and external wiring shielding to minimize electromagnetic noise. The data were collected, and the relays and heater current were controlled, via a separate PC to the PPMS control computer, utilizing a flexible and modular instrument control framework running in MATLAB.

Figure 5 gives a schematic of the wiring and ground connections employed. The three-terminal shielded connections detailed in the AH Bridge manual were used—the shielded coaxial cable is run down the length of the probe to the sample puck. At this stage, the coaxial cable cores are soldered to the pins that connect to the puck, and the braided shields are connected to the radiation shield (which is electrically isolated from the PPMS puck and hence the PPMS ground and additionally the rest of the probe). The radiation shield then serves as an electrically shielded environment, and the shields of each coaxial cable are joined together only at a position as close to the sample as possible, as mandated by the three-terminal method.

IV. EXPERIMENTAL PERFORMANCE AND UNCERTAINTIES

A. Thermometer resolution and self-heating

Resolution of the temperature measurements depends on the temperature sensitivity of the capacitive thermometer and resolution of the capacitance measurement. The expected temperature resolution (temperature dependent) was calculated for an example of one of the thermometers used. The measured temperature dependent capacitance and the sensitivity of the thermometer are shown

in Fig. 6(a). The capacitance resolution (capacitance dependent) was taken from the AH Bridge manual, and from this, temperature resolution was calculated, as shown in Fig. 6(b). In the optimal range 2–100 K, temperature resolution is found to be better than 0.1 mK. SrTiO₃ exhibits a maximum in the dielectric constant around 2 K,²⁸ but the magnitude of the signal is such that the resolution remains extremely high until very close to this turning point. We also note that while 2–100 K is the most effective range, milliKelvin resolution is in principle possible up to room temperature—but other uncertainties can be expected to dominate at this point. Preliminary tests have yielded usable data up to 150 K at the time of writing. The inset in Fig. 6(b) shows an approximate comparison with the electronic resolution of Cernox resistive thermometers from Lakeshore Cryotronics, Inc., measured on a Lakeshore 372 resistance bridge. We use the resolution values supplied by Lakeshore, with the excitation current range set to give self-heating on a similar order of magnitude to the capacitive thermometers. We note that real-world resolution will be further affected by Johnson noise and magnetoresistance errors, factors not existent in the capacitive setup—even without these, the capacitance measurement shows greater resolution at all but the lowest temperature ranges.

The calculated electronic temperature resolution of the measurement shown in Fig. 6(b) does not capture the full picture of the uncertainties since measurement of capacitance can be affected by vibration of components or other parasitic capacitances, temperature or field drift, calibration errors, etc. It is important to gain an empirical measure of the real-world performance with all these factors. This is additionally complicated by the fact that averaging multiple points in the steady state and compensation for effects such as linear drifts can, conversely, improve data accuracy beyond the electronic resolution of a single point. In our test experiments, an example of which we show in Sec. IV B, we succeeded in reproducibly resolving temperature differences of the same order as the expected electronic resolution [plotted as pink diamond in Fig. 6(b)]. Further capacitance noise analysis demonstrated that we are able to achieve real experimental resolution at the level of the expected electronic resolution limit.

We further delineate our measurement performance by calculating the minimum thermal Hall angle ratio $\kappa_{xy}/\kappa_{xx} = (L_x/L_y)(\Delta T_y/\Delta T_x)$ measurable on our setup. This dimensionless quantity is independent of sample conductivity and geometry, as well as experimental parameters, and gives a clear indication of the size of a thermal Hall signal in a given sample for comparisons. Allowing ΔT_x to be 5% of the sample temperature and using the temperature resolution of Fig. 6(b) as the limit on ΔT_y , we can calculate the lower bound of the measurable thermal Hall angle ratio—this is plotted in Fig. 6(c), along with the reported thermal Hall angle ratio values of various previously measured insulating samples. As can be seen, within the full 2–300 K temperature range, our measurement setup can cover all the existing samples found in the literature. Moreover, we were able in subsequent tests to measure a thermal Hall angle ratio of 5×10^{-5} over the wide temperature range 40–150 K.

Self-heating or effective power consumption, of each capacitive thermometer, was calculated using the following expression:

$$P_e = I^2 \times ESR = \frac{V^2 ESR}{ESR^2 + (\omega C)^{-2}}. \quad (4)$$

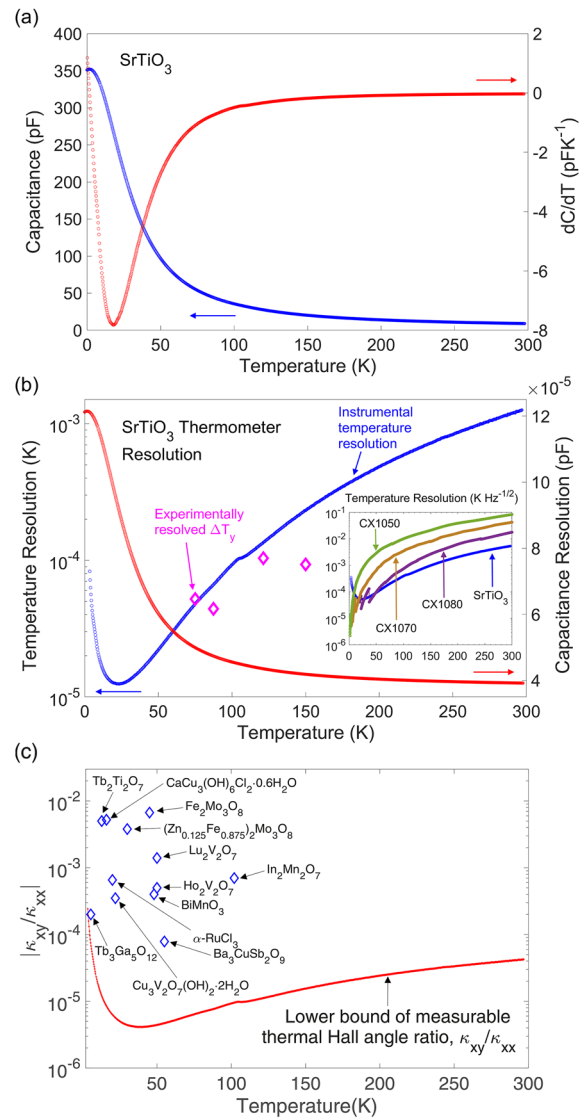


FIG. 6. (a) Measured capacitance (blue, left axis) and its derivative dC/dT (red, right axis) plotted against temperature for one of the SrTiO₃ thermometers used. (b) Calculated capacitance (red, right) and temperature (blue, left) resolution as functions of temperature, calculated from the measured dC/dT values and the AH Bridge precision (capacitance-dependent) for the measurement parameters used—including the time constant detailed in Sec. V A. From 2 to 100 K, temperature resolution beyond 0.1 mK is predicted. Values for smallest resolved transverse temperature differences are overlaid onto the calculated instrumental temperature resolution curve (pink diamonds), taken from test measurements (temperature recordings with average time set to 7 s were collected over 15 min and averaged for each measurement point). The inset shows comparisons with the electronic temperature resolution of Cernox resistive thermometers, using an LS372 bridge and a 316 nA range to keep self-heating on the order of the capacitance thermometers. For proper comparison, difference of time constant was considered and resolutions were normalized by $\sqrt{\text{Hz}}$. (c) Lower bound of the measurable thermal Hall angle ratio κ_{xy}/κ_{xx} , extracted from the calculated temperature resolution and test measurements, plotted against temperature. Reported typical κ_{xy}/κ_{xx} values for each insulating material currently reported in the literature^{2,5,10,24} are plotted as blue diamonds for comparison—all fall well within the accessible range.

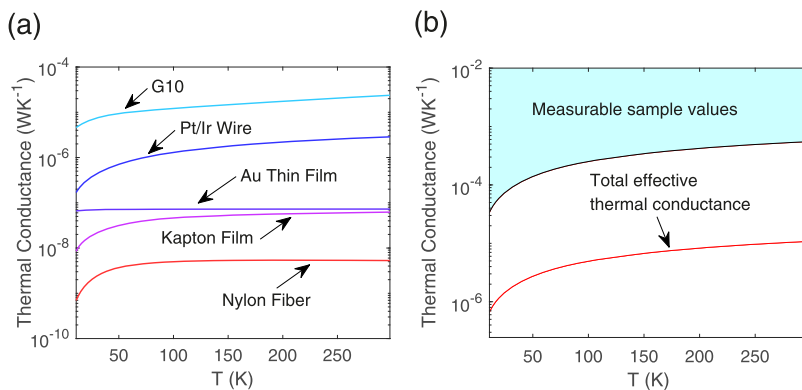


FIG. 7. (a) Calculated thermal conductance through the Kapton ribbons and other elements of the thermal isolation structure. (b) Calculated total effective thermal conductance through all secondary channels. The shaded region denotes the minimum sample thermal conductances measurable while keeping secondary heat channel errors below 2%.

ESR stands for effective series resistance and can be measured simultaneously with capacitance by the AH Bridge (with unit option kOhm). Calculated thermometer self-heating was below 7.5 nW for the temperature range of 2–300 K and below 1 nW for the temperature range of 25–300 K; self-heating of the thermometers can be considered a negligible effect.

B. Heat losses

Systematic temperature errors exist when measuring thermal transport properties from heat loss through secondary channels—the system can never be perfectly isolated from its surroundings, particularly as wiring connections must be made to various components. Temperature-dependent heat loss through each secondary channel was calculated quantitatively. Heat loss is independently possible through the Kapton film and evaporated gold film within the Kapton ribbon, and also through the fiberglass posts, Pt/Ir wire, and nylon support fibers. Thermal conductivity values of nonmetallic components were extracted from the Cryocoolers Conference Proceedings²⁹ and the Wiedemann-Franz law³⁰ together with the manufacturer's specifications (Goodfellow) used to calculate thermal conductivity for the metallic components. The calculated temperature-dependent thermal conductance of each secondary channel, including the heater and all three thermometer connections and leads, is shown in Fig. 7(a), and the calculated total effective thermal conductance through them all is shown in Fig. 7(b). If the sample conductance is within the shaded blue region above the cutoff line shown, the error from the heat leak through the secondary channel is within 2%. These considerations include a weak heat loss channel through its wiring for heat generated in the heater. The result of this particular loss, however, will merely be a smaller heater power than anticipated flowing through the sample, scaling multiplicatively any temperature differences observed. This has no effect on resolution or relative changes in thermal Hall signals observed, merely scales the absolute values recorded—but we include it in this calculation to give a worst-case estimate.

V. EXAMPLE EXPERIMENTAL RESULTS

To verify our instrument works as intended and to assess its resolution and any systematic errors, we reproduced previously

published data on reference samples, and additionally measured a control sample with no thermal Hall effect to eliminate the possibility of experimental artifacts being responsible for the measured signals.

A. Tb₂Ti₂O₇ experimental data

To test the performance of our setup in measuring the thermal Hall effect, we reproduced results from the data of Hirschberger *et al.*⁴ on pyrochlore insulating antiferromagnet Tb₂Ti₂O₇. This material was shown by Hirschberger to have a significant κ_{xy} due to an exotic quantum spin ice ground state, and a large signal in the optimal resolution range of our setup, making it an ideal test sample.

We aligned a high-purity single crystal of Tb₂Ti₂O₇ to have the [1 1 1] crystallographic direction perpendicular to the sample plane (i.e., along *z*, as with the setup of Hirschberger) and cut to size 1.48 × 4.53 × 0.39 mm³ with a diamond wheel. Thermal contacts were made for the 3 thermometers by bonding the silver wire to the clean crystal surface using the Epotek 2-part silver-loaded epoxy. The sample mounted on the measurement puck is that pictured in Fig. 3. We chose to take a detailed set of field-dependent measurements at 30 K. We cooled the system to 30 K in a helium exchange-gas atmosphere, performed an *in situ* calibration of the thermometers from 30 to 33 K, and then evacuated the sample chamber after ensuring all temperatures had reached stable equilibrium values and hence all residual heat had been removed. After reaching high vacuum conditions, enabling the heater with the desired power and again waiting for stability, measurements were taken by setting fixed magnetic fields and collecting data for around 20 min at each field. A slow continuous ramping of magnetic field was found to give equivalent results, but for the purpose of this test, we wished to rule out magnetocaloric heating effects by ensuring that the temperatures had stabilized at each field point. A constant temperature was then fitted to each set of points at each field using a least-squares regression, and the uncertainty in this fit combined with uncertainties in capacitance determination and the calibration interpolation yield experimental uncertainties of order 0.1 mK. The field-dependent ΔT_x and ΔT_y values were extracted from symmetrizing and antisymmetrizing the resulting temperature differences between thermometers 1 and average of 2, 3, and between 2 and 3—the variations of temperatures with field are shown in Fig. 8.

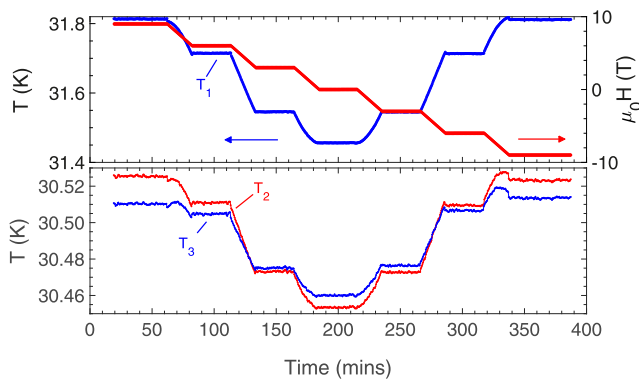


FIG. 8. $\text{Tb}_2\text{Ti}_2\text{O}_7$ raw experimental data showing the 3 temperature readings and magnetic field plotted against time, with a heater power of $300 \mu\text{W}$. The upper panel shows the temperature recorded by thermometer 1 in blue, left axis, and the applied magnetic field, red, right axis plotted against time. The lower panel shows the temperatures recorded by thermometers 2 (red) and 3 (blue) plotted on the same time axis as the upper panel. All temperatures are seen to be stable at the intervals where the field is held constant for measurement.

Figure 9(a) shows the resulting ΔT_y values for separate field-dependent measurements with set heater powers of 0, 100, 200, 300, and $400 \mu\text{W}$. ΔT_y was seen to increase linearly with field, and the magnitude of this temperature difference was seen to scale linearly with heater power, as expected. With the heater turned off, zero signal was measured well within experimental uncertainty. The data taken with $400 \mu\text{W}$ slightly diverge from linear behavior, as the ΔT_x values start to become too large, above 5%, and distort the data—this heater power was close to being too high for this sample. Using Eqs. (2) and (3) allows determination of the longitudinal and transverse thermal conductivity terms κ_{xx} and κ_{xy} —these are plotted, divided by temperature, in Fig. 9(b). The data show excellent agreement with the form of those of Hirschberger *et al.*⁴ but with slightly higher magnitudes of the conductivities, potentially due to better sample quality. The signal is very clearly resolvable above the noise and uncertainties, giving confidence that our setup is well equipped to measure thermal Hall signals of this size and indeed significantly smaller ones.

B. Control sample experimental data

To confirm further that the thermal Hall signals we observe were intrinsic properties of sample, rather than some artifacts of the experimental setup such as the thermal conductance of the silver wires used, we carried out measurements under the exact same experimental conditions as for $\text{Tb}_2\text{Ti}_2\text{O}_7$ on a nonmagnetic control sample—a piece of glass. We cut down and polished a standard microscope slide to the same dimensions as the $\text{Tb}_2\text{Ti}_2\text{O}_7$ single crystal—such glass was chosen as its thermal conductivity is similar to that of $\text{Tb}_2\text{Ti}_2\text{O}_7$, so thermal gradients and experimental conditions would be as similar as possible. The measurement results (with $200 \mu\text{W}$ of heater power), black left-pointing triangles in Fig. 9(a), showed ΔT_y with no clear field dependence, and magnitude of zero well within the experimental uncertainties of 0.1 mK. We can then be confident that any signal we measure is intrinsic to the sample, rather than experimental artifacts.

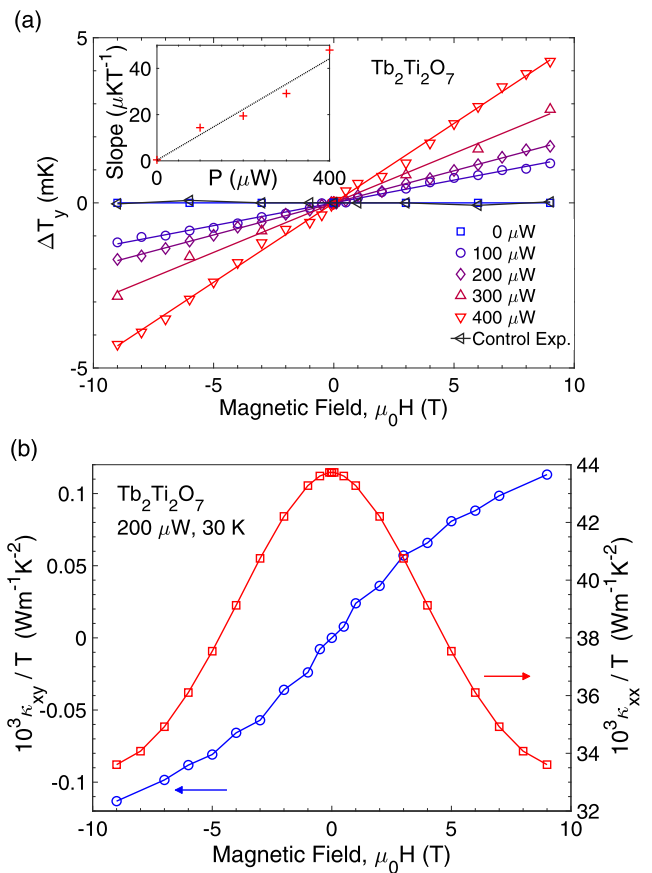


FIG. 9. (a) ΔT_y extracted transverse temperature difference at 30 K for the $\text{Tb}_2\text{Ti}_2\text{O}_7$ sample, plotted against the applied field for different heater powers. The data show good agreements to linear fits, shown as solid lines. The slopes of these fits scale linearly with applied heater power, as shown in the inset. When no heater power was applied, no measurable signal was observed. Data from the glass control sample (control experiment) are also shown as black left-pointing triangles, giving again no signal within error. (b) Extracted κ_{xx} and κ_{xy} values, divided by temperature, for the $200 \mu\text{W}$ data at 30 K, plotted against applied magnetic field.

VI. DISCUSSION

We have demonstrated a cheap and easy to build top-loading probe designed to be loaded into a widely available Quantum Design PPMS cryostat, with a detachable shielded sample puck section and robust heat sinking of three pairs of coaxial cables. The modular puck design has a radiation shield for thermal isolation and protection of the delicate sample space while handling and allows any variety of experimental setup benefiting from shielded coaxial wiring to be constructed on a sample puck. Pucks can be quickly and easily switched, and the system makes use of the simple yet extremely stable temperature and magnetic field control of the easy-to-use PPMS system. We focus on a setup designed for measurements of the thermal Hall effect and show that this system can yield unprecedented resolution of these data, over a wide temperature range and with rapid sample mounting or changing—allowing a large collection of potential samples to be screened for this novel physics.

ACKNOWLEDGMENTS

The authors would like to thank Seong-Il Choi, Nahyun Lee, Suhan Son, Inho Hwang, Junghyun Kim, S. S. Saxena, C. Liu, and D. Jarvis for their generous help, technical expertise, and discussions. We would also like to acknowledge support from the Jesus College of the University of Cambridge. This work was supported by the Institute for Basic Science (IBS) in Korea (Grant No. IBS-R009-G1) and EPSRC in UK (Grant No. EP/M028771/1).

REFERENCES

- ¹Y. Kasahara, T. Ohnishi, Y. Mizukami, O. Tanaka, S. Ma, K. Sugii, N. Kurita, H. Tanaka, J. Nasu, Y. Motome, T. Shibauchi, and Y. Matsuda, *Nature* **559**, 227 (2018).
- ²Y. Kasahara, K. Sugii, T. Ohnishi, M. Shimozawa, M. Yamashita, N. Kurita, H. Tanaka, J. Nasu, Y. Motome, T. Shibauchi, and Y. Matsuda, *Phys. Rev. Lett.* **120**, 217205 (2018).
- ³D. Watanabe, K. Sugii, M. Shimozawa, Y. Suzuki, T. Yajima, H. Ishikawa, Z. Hiroi, T. Shibauchi, Y. Matsuda, and M. Yamashita, *Proc. Natl. Acad. Sci. U. S. A.* **113**, 8653 (2016).
- ⁴M. Hirschberger, J. Krizan, R. Cava, and N. Ong, *Science* **348**, 106 (2015).
- ⁵H. Doki, M. Akazawa, H.-Y. Lee, J. H. Han, K. Sugii, M. Shimozawa, N. Kawashima, M. Oda, H. Yoshida, and M. Yamashita, *Phys. Rev. Lett.* **121**, 097203 (2018).
- ⁶R. Hentrich, M. Roslova, A. Isaeva, T. Doert, W. Brenig, B. Büchner, and C. Hess, *Phys. Rev. B* **99**, 085136 (2018); e-print [arXiv:1803.08162v1](https://arxiv.org/abs/1803.08162v1).
- ⁷M. Hirschberger, R. Chisnell, Y. Lee, and N. Ong, *Phys. Rev. Lett.* **115**, 106603 (2015).
- ⁸T. Ideue, Y. Onose, H. Katsura, Y. Shiomi, S. Ishiwata, N. Nagaosa, and Y. Tokura, *Phys. Rev. B* **85**, 134411 (2012).
- ⁹Y. Onose, T. Ideue, H. Katsura, Y. Shiomi, N. Nagaosa, and Y. Tokura, *Science* **329**, 297 (2010).
- ¹⁰K. Sugii, M. Shimozawa, D. Watanabe, Y. Suzuki, M. Halim, M. Kimata, Y. Matsumoto, S. Nakatsuji, and M. Yamashita, *Phys. Rev. Lett.* **118**, 145902 (2017).
- ¹¹C. Strohm, G. Rikken, and P. Wyder, *Phys. Rev. Lett.* **95**, 155901 (2005).
- ¹²A. V. Inyushkin and A. N. Taldenkov, *JETP Lett.* **86**, 379 (2007).
- ¹³K. van Hoogdalem, Y. Tserkovnyak, and D. Loss, *Phys. Rev. B* **87**, 024402 (2013).
- ¹⁴H. Katsura, N. Nagaosa, and P. Lee, *Phys. Rev. Lett.* **104**, 066403 (2010).
- ¹⁵M. Kawano and C. Hotta, *Phys. Rev. B* **99**, 054422 (2018); e-print [arXiv:1805.05872v2](https://arxiv.org/abs/1805.05872v2).
- ¹⁶S. Kim, K. Nakata, D. Loss, and Y. Tserkovnyak, *Phys. Rev. Lett.* **122**, 057204 (2018); e-print [arXiv:1808.06690v1](https://arxiv.org/abs/1808.06690v1).
- ¹⁷H. Lee, J. Han, and P. Lee, *Phys. Rev. B* **91**, 125413 (2015).
- ¹⁸J. Nasu, J. Yoshitake, and Y. Motome, *Phys. Rev. Lett.* **119**, 127204 (2017).
- ¹⁹S. Owerre, e-print [arXiv:1811.01946v2](https://arxiv.org/abs/1811.01946v2) (2018).
- ²⁰K.-S. Kim, K. H. Lee, S. B. Chung, and J.-G. Park, *Phys. Rev. B* **100**, 064412 (2018); e-print [arXiv:1811.11201v1](https://arxiv.org/abs/1811.11201v1).
- ²¹K. H. Lee, S. B. Chung, K. Park, and J.-G. Park, *Phys. Rev. B* **97**, 180401 (2018).
- ²²C. Tinsman, G. Li, C. Su, T. Asaba, B. Lawson, F. Yu, and L. Li, *Appl. Phys. Lett.* **108**, 261905 (2016).
- ²³C. Strohm, "Magneto transverse phonon transport," Ph.D. thesis, 2003.
- ²⁴T. Ideue, T. Kurumaji, S. Ishiwata, and Y. Tokura, *Nat. Mater.* **16**, 797 (2017).
- ²⁵S. Ghannadzadeh, M. Coak, I. Franke, P. Goddard, J. Singleton, and J. Manson, *Rev. Sci. Instrum.* **82**, 113902 (2011).
- ²⁶Y. Shiomi, R. Takashima, and E. Saitoh, *Phys. Rev. B* **96**, 134425 (2017).
- ²⁷M. Coak, "Quantum tuning and emergent phases in charge and spin ordered materials," Ph.D. thesis, University of Cambridge, 2017.
- ²⁸S. Rowley, L. Spalek, R. Smith, M. Dean, M. Itoh, J. Scott, G. Lonzarich, and S. Saxena, *Nat. Phys.* **10**, 367 (2014).
- ²⁹IC Conference, *Cryocoolers 11*, edited by J. R. G. Ross (Kluwer Academic, 2002).
- ³⁰R. Franz and G. Wiedemann, *Ann. Phys. Chem.* **165**, 497 (1853).